Estuarine, Coastal and Shelf Science 203 (2018) 29–43

Contents lists available at ScienceDirect

Estuarine, Coastal and Shelf Science

journal homepage: www.elsevier.com/locate/ecss

Moderate effect of damming the Romaine River (Quebec, Canada) on coastal plankton dynamics

Simon Senneville [a, *], Irene R. Schloss [a, b, c], Simon St-Onge Drouin [a], Simon Bélanger [d], Gesche Winkler [a], Dany Dumont [a], Patricia Johnston [e], Isabelle St-Onge [e]

[a] Institut des sciences de la mer de Rimouski et Québec-Océan, Université du Québec à Rimouski, 310 allée des Ursulines, C.P. 3300, Rimouski, Québec, G5L 3A1, Canada
[b] Instituto Antártico Argentino, Buenos Aires, Argentina
[c] Centro Austral de Investigaciones Científicas, CONICET and Universidad Nacional de Tierra del Fuego, Ushuaia, Argentina
[d] Département de biologie, chimie et géographie, groupe BORÉAS et Québec-Océan, Université du Québec à Rimouski, 300 allée des Ursulines, Rimouski, Québec, G5L 3A1, Canada
[e] Hydro-Québec, Innovation, équipement et services partagés, Unité environnement, 855 rue Ste-Catherine Est, 11e étage, Montréal, Québec, H2L 4P5, Canada

ARTICLE INFO

Article history:
Received 21 June 2017
Received in revised form
29 January 2018
Accepted 2 February 2018
Available online 3 February 2018

Keywords:
Biophysical modelling
River damming
Plankton
Light attenuation
Canada
Québec
Mingan archipelago

ABSTRACT

Rivers' damming disrupts the seasonal cycle of freshwater and nutrient inputs into the marine system, which can lead to changes in coastal plankton dynamics. Here we use a 3-D 5-km resolution coupled biophysical model and downscale it to a 400-m resolution to simulate the effect of damming the Romaine River in Québec, Canada, which discharges on average 327 $m^3 s^{-1}$ of freshwater into the northern Gulf of St. Lawrence. Model results are compared with environmental data obtained from 2 buoys and *in situ* sampling near the Romaine River mouth during the 2013 spring–summer period. Noteworthy improvements are made to the light attenuation parametrization and the trophic links of the biogeochemical model. The modelled variables reproduced most of the observed levels of variability. Comparisons between natural and regulated discharge simulation show differences in primary production and in the dominance of plankton groups in the Romaine River plume. The maximum increase in primary production when averaged over the inner part of Mingan Archipelago is 41%, but 7.1% when the primary production anomaly is averaged from March to September.

1. Introduction

Although coastal regions are amongst the most productive ecosystems on the planet (Gazeau et al., 2004), the lower Estuary of St. Lawrence presents relatively low annual planktonic primary production (Cloern et al., 2014), with values of 100 g C m^{-2} yr^{-1}. High seasonality characterizes the Estuary and Gulf of St. Lawrence (EGSL), in addition to a cyclonic estuarine circulation, strong and deep (>100 m) wind-induced mixing during the cold and darker winter, continuous tidal mixing, and frequent upwelling events forced by dominant westerly winds along the northern coast (Bourque and Kelley, 1995). Stratification resulting from surface warming and vernal irradiance favour sustained primary productivity during summer and fall (Le Fouest et al., 2005, 2006).

On the northern coast of the Gulf of St. Lawrence, several rivers enter the Gulf. Among them, the Romaine River, a 300 km long river that originates near the Québec–Labrador border (Fig. 1). It discharges into the Mingan Archipelago on the northern shore of the Gulf of St. Lawrence. The Romaine River drains a 14 500 km^2 basin, and has a mean annual runoff of 327 $m^3 s^{-1}$ (μSv). Plankton production in the northern Gulf of St. Lawrence (GSL) and in the area around Jacques Cartier Strait, including the Mingan Archipelago, is supported by the supply of nutrient-rich water of oceanic origin, with nitrate concentrations ranging from 0.0 to 12.5 μM, and an overall mean of 6.5 μM (Plourde and Therriault, 2004). Nitrate concentrations of the Romaine River are low all year long (0.07 ± 0.06 μM; Hydro-Québec, 2007). However, other estimates indicate that nitrate content can reach up to 3.5 μM during spring freshet with an annual average of 1.5 ± 0.9 μM (S. Bélanger, unpublished results). No measure of primary production in this

* Corresponding author.
E-mail address: simon_senneville@uqar.ca (S. Senneville).

https://doi.org/10.1016/j.ecss.2018.02.006
0272-7714/

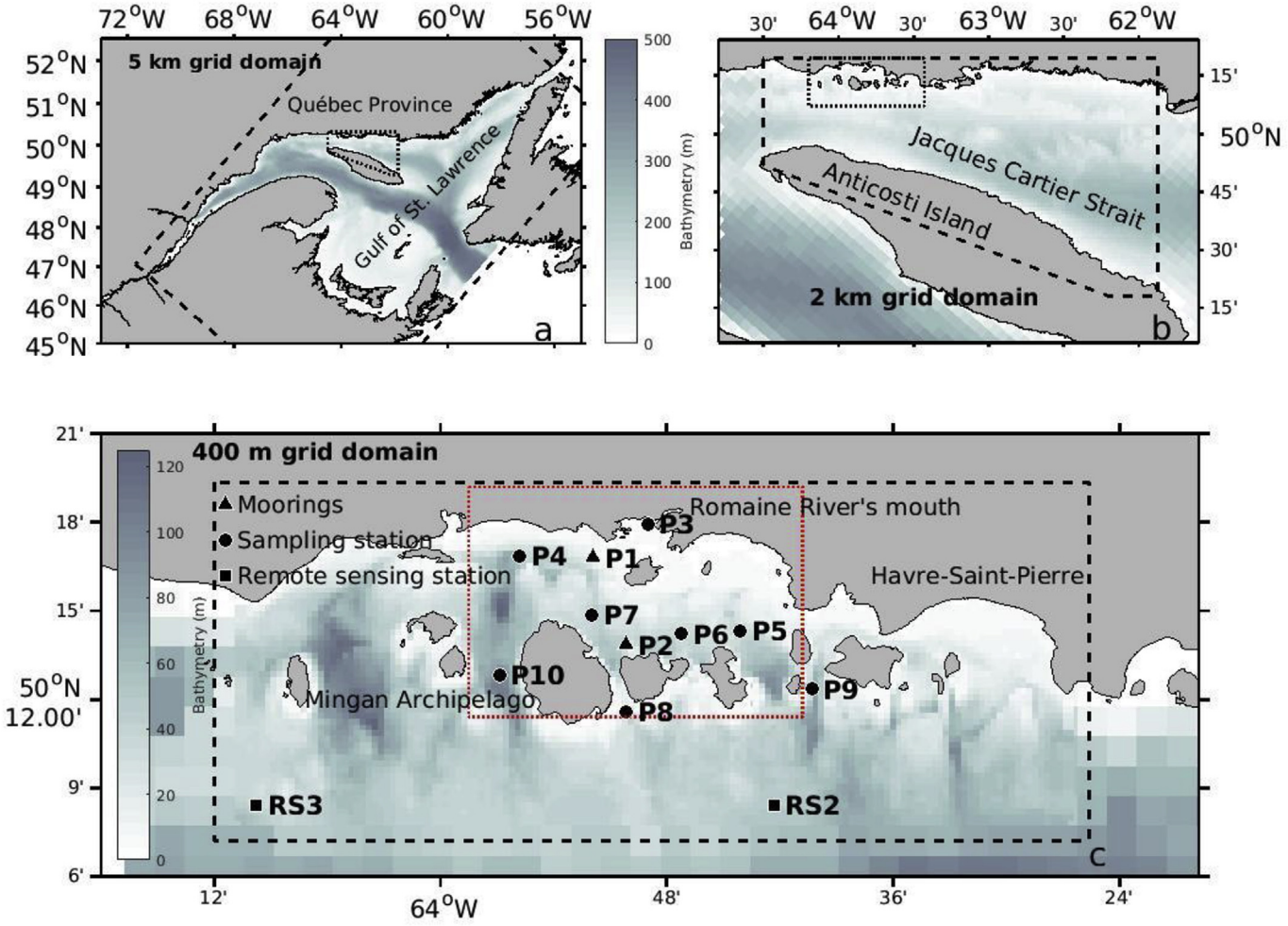

Fig. 1. Bathymetric maps (m) showing station positions and the different model domains. a) The 5 km grid domain (dotted line); b) the 2 km grid domain between Anticosti Island and the North Shore; c) the 400 m grid section in the Mingan Archipelago. Panel c shows the 10 sampling stations (P1 to P10), including the two mooring stations (P1, P2) and the two remote sensing stations (RS2, RS3). The red square corresponds to the domain where most of the analyses were done. (For interpretation of the references to colour in this figure legend, the reader is referred to the Web version of this article.)

relatively small area exists, although modelling studies estimated production rates as high as 150 g C m^{-2} yr^{-1} for the Jacques Cartier area (Le Fouest et al., 2005).

In 2009, Hydro-Quebec began the construction of a 1550 MW hydroelectric complex on the Romaine River. The complex of four generating stations fed by reservoirs is slated for completion in 2020, and the first generating station was commissioned in December 2014. Creating and managing the four Romaine complex reservoirs will modify the hydrologic and hydraulic regimes of the river. The mean annual discharge would remain the same, but seasonality would change markedly. In general, the normally low summer and winter discharges will be higher compared to natural conditions, while spring and fall freshets will be considerably dampened (Jaegler, 2014; Hydro-Québec, 2007). Nevertheless, discharge peaks may still occur during the spring flood period, potentially affecting phytoplankton dynamics in coastal areas near river mouths (Domingues and Galvao, 2007).

In situ sampling, satellite remote sensing, ecosystem modelling, or a combination of these different methodological approaches can be used to study the impact of river waters on plankton in coastal waters. 3-D hydrodynamic models are the only tools that provide the necessary temporal and spatial resolutions to capture an integrated view of the physical processes on which plankton strongly depends. We will use these tools to test our main hypothesis that the damming of the Romain River should not have a significant effect on the primary production in the Mingan Archipelago. In addition, we will show that, light and biogeochemical parameterizations traditionally used in conjunction with 3-D circulation models need to be inspected and adapted to shallow coastal and river-influenced environments; they require modifications with regards to the presence of dissolved and particulate matter that greatly affect the light field in the water column and, hence, primary production. In this study, i) we present and discuss *in situ* data from spring −summer 2013 collected around the Romaine River mouth and Mingan Archipelago in natural conditions, ii) we compare these results with the outputs of a coastal domain model downscaled from an existing biophysical model (Saucier et al., 2003), coupled with a NPZD model (Le Fouest et al., 2005, 2006) for the Gulf of St. Lawrence, in which we explicitly consider the effect of coloured dissolved and particulate organic matter on light attenuation in coastal waters, and iii) we simulate the impact of damming the Romaine River on plankton production, providing overall a method for similar studies in other river-influenced systems. The ultimate objective of our work is to study the effect of river damming on coastal plankton biomass and production in the northern GSL.

2. Materials and methods

2.1. Field sampling

Field data were acquired as part of Hydro-Québec monitoring activities. These included continuous data from sensors on buoys, discrete field sampling, and satellite remote sensing data. The study area is located west of Havre-Saint-Pierre (Québec) in the channel of the Mingan Islands. Ten sampling stations (P1 to P10; Fig. 1c) at various distances from the Romaine River mouth were selected to track physicochemical variables and plankton parameters in the water column. Two buoys equipped with a series of instruments (Table 1) installed 1 m below the surface were deployed at stations P1, which is located near the mouth of the Romaine River, and P2, which is between two islands of the Mingan Archipelago. All ten stations were visited monthly between April and September 2013. In addition, two virtual stations were identified that correspond to the locations of the highest-quality remote sensing data available for that season (RS2 and RS3; Fig. 1c).

For the first two sampling dates, data (temperature, salinity, chlorophyll-*a*, and dissolved oxygen) were collected at discrete depths from the surface down to 50 m (0.5, 1.5, 2.5, 5, 7.5, 10, 12.5, 15, 20, 25, 30, 35, 40, 45, and 50 m) at each of the 10 stations. A multiparameter YSI EDS6600 probe was used during April and May sampling campaigns and a RBR-XRX-420 probe was used from June on. PAR attenuation in the water column was measured using LICOR sensors at the surface (LI-250) and underwater (LI-193), respectively. During the campaigns from June on, the RBR-XRX-420 probe was used to monitor temperature, salinity, turbidity, chlorophyll-*a* fluorescence (chl-*a*), and dissolved oxygen every ~0.25 m from the surface to 50 m depth.

During each of the monthly sampling campaigns, discrete water samples were collected at the 10 stations using a Niskin bottle. Water was sampled at three depths: 1.5 m, at depth corresponding to 10% of surface irradiance since no clear chl-*a* maximum was evident and 3 m over the bottom. Chl-*a* and nutrient concentrations as well as phytoplankton taxonomic composition were analyzed. Duplicate samples were taken for chl-*a* and nutrients, which were analyzed at Maxxam Analytic Laboratory (Ville St-Laurent, Québec), while plankton analyses (see below) were performed at the Institut des sciences de la mer de Rimouski (ISMER). Phytoplankton and microzooplankton samples were taken in duplicate from the surface and at the 10% irradiance depth for all stations, fixed with acidic Lugol's solution at a ratio of 1 mL–250 mL of sample, and stored in dark conditions at 4 °C until analysis. In addition, integrated water-column samples from 5 m over the bottom to the surface for zooplankton analyses were taken with a ring net (150 μm mesh size, 0.75 m diameter) equipped with a flowmeter. Zooplankton samples were fixed with 95% ETOH at a 3:1 ethanol:zooplankton volume ratio and kept in cold and dark conditions for 24 h after which 100% of the ethanol was replaced by fresh 95% ETOH.

2.2. Phytoplankton and microzooplankton analyses

Phytoplankton and microzooplankton samples were analyzed using both a FlowCam and by inverted microscopy.

FlowCam analysis: Subsamples of 6 mL per sample were analyzed with a 10× objective (corresponding to a magnification 100×) using a Bench Top FlowCAM® VS IV. The flow was 0.18 mL min^{-1}, and 20 frames per second were considered. Classification of cell sizes was done by analyzing particles in the images according to the Area Based Diameter principle (ABD). All samples were analyzed in duplicate and the average concentration per size class was calculated. The minimum size of the analyzed particles was 4 μm. Organisms were classified into four groups based on their size: 4–< 10 μm, 10–< 20 μm, 20–<50 μm, and 50–300 μm.

Analysis by inverted microscopy: Each 100 mL sample was sedimented in an Utermöhl (1958) sedimenting chamber for 24 h before analysis under an inverted microscope (Wild M40). Cells on six transects were quantified (three transects at a magnification up to 100× and three transects at a magnification up to 400× or more), so that the minimum number of particles exceeded 500 cells. Organisms were classified into the following categories: centric diatoms, pennate diatoms, dinoflagellates, other flagellates, ciliates, and choanoflagellates. Except for choanoflagellates, each group was quantified by size class (0–< 5 μm, 5–< 10 μm, 10–< 20 μm, 20–50 μm, and >50 μm). We analyzed 29 samples that had the highest phytoplankton abundances. Diatoms and autotrophic flagellates smaller than 5 μm are considered as small phytoplankton (SP), while the larger autotrophic organisms are grouped as large phytoplankton (LP). Heterotrophic microplankton are grouped as microzooplankton (SZ).

Phytoplankton carbon was estimated using cell size and shape to calculate cell volume (Montagnes et al., 1994). This conversion was done based on the size/volume of the organisms and conversion factor from the literature (Menden-Deuer and Lessard, 2000; Hillebrand et al., 1999). Total carbon was determined for phytoplankton <5 μm, phytoplankton >5 μm, and microzooplankton.

2.3. Zooplankton analyses

A total of 42 zooplankton samples were analyzed under a Leica stereo microscope. Four stations were sampled in duplicate in April while seven were sampled in duplicate from May through September. Organisms were classified according to the taxonomic groups presented in Annex I and according to two size classes, 150 μm–1 mm and >1 mm.

Table 1
Sensors on the P1 and P2 buoys.

Sensor	Variable	Range, units, error
Satlantic SUNA	Nitrates	7–56 000 μg l^{-1} ± 1(μg L^{-1})
Franatech	Dissolved CO_2	0–50 000 ppm ± 5%
RBR-XRX-420	Temperature (water)	-5–35 °C ± 0.002 °C
RBR-XRX-420	Conductivity	0–150 mS cm^{-1} ± 0.003 mS cm^{-1}
Seapoint Turbidity (coupled to XRX-420)	Turbidity	0–750 NTU ± 2%
Seapoint Fluorometer (coupled to XRX-420)	chl-a	0.02–150 μg L^{-1} ± 2%
JFE Alec RINKO III (coupled to XRX-420)	Dissolved oxygen	0–20 mg L^{-1} ± 2%
Weatherpak 2000 (P2 only)	Wind speed	0–60 m s^{-1} ± 0.1 m s^{-1}
Weatherpak 2000 (P2 only)	Wind direction	
Weatherpak 2000 (P2 only)	Temperature (air)	−40–100 °C ± 0.1 °C
Weatherpak 2000 (P2 only)	Humidity	0–100% ± 1%
Weatherpak 2000 (P2 only)	Atmospheric pressure	500–1200 mbar ± 2 mbar

For the 150 μm–1 mm fraction, subsamples were counted (between 5 and 10% of the sample) so that the minimum number of individuals exceeded 300 individuals, except for one sample (03/07/2013 at P3), which contained almost nothing but fine sediment. The complete >1 mm fraction was counted. Zooplankton abundance per station, expressed in numbers per m^3, was calculated as an average of the two zooplankton samples. The sum of the two fractions resulted in the total abundance of mesozooplankton per m^3.

To estimate the total carbon from zooplankton, biovolume and carbon content were calculated for the dominant organisms (i.e., those present in more than 10% of the samples with abundances > 10 ind m^{-3}) based on values from the literature and own unpublished results (Table 2). To compare field results with model output, zooplankton abundance data for the 12 and 14 most abundant taxa, corresponding to the small (150–1000 μm) and large (>1000 μm) organisms, respectively, was converted into carbon according to species. The number of retained taxa was determined by considering the groups that were present in at least 10% of the samples with abundances higher than 600 ind m^{-3} for the 150–1000 μm fraction and 10 ind m^{-3} for the >1000 μm fraction. The complete list of taxa and is presented in Annex 1.

2.4. Satellite remote sensing

Satellite data from MODIS-Aqua were downloaded from the NASA-OBPG web site at level 1A (1 km resolution) and processed to level 2 using the SeaDAS 7.0 software. We applied the atmospheric correction scheme for turbid waters developed by the MUMM (department of the Royal Belgian Institute of Natural Sciences) (Ruddick et al., 2000, 2006), which is more suitable than standard NASA algorithms over moderately turbid coastal waters. Several empirical and semi-analytical algorithms were tested to estimate the diffuse attenuation coefficient of PAR (K_{PAR}) and surface chl-*a*. Based on the limited set of concomitant remote sensing and *in situ* measurements (not shown), the best algorithm for K_{PAR} was the quasi-analytical algorithm of Lee et al. (2002, 2005), while the standard algorithm for chl-*a* (OC3) was retained for waters outside the river plume.

2.5. The 3-D regional model for the St. Lawrence system

2.5.1. Downscaling

The model used for the simulations was derived from the coupled ice–ocean circulation model of the Gulf of St. Lawrence developed by Saucier et al. (2003, 2004). In 2011, this model became the oceanic component of the GEM (Global Environmental Multiscale Model), which is the Canadian operational meteorological forecasting system (Pellerin et al., 2004). For each cell (node) of the grid, the independent state variables were calculated on discrete time steps ranging from 300 s for the 5 km grid to 30 s for the 0.4 km grid. The model also considered freshwater input from coastal tributaries as well as exchanges with outer waters of the Gulf of St. Lawrence for tides and salt and heat transport.

The complex coastline and bathymetry of the Mingan Archipelago, where the Romain River ends, is not well resolved by the 5 km grid. We thus adopted a one-way nesting approach to downscale the physical processes at a progressively finer scale from 5 to 2 km, and then from 2 to 0.4 km (Fig. 1), respecting a maximum ratio of 5:1 for each nesting procedures (Spall and Holland, 1991).

2.5.1.1. Model configuration and forcing. The 5 km simulation runs from December 2012 to December 2013 (including ice dynamics) while the 2 km simulation runs from 5 March 2013—as soon as sea ice left the domain (concentration less than 2%)—until December 2013. Finally, the 0.4 km simulation runs from 15 March 2013, to allow for the spin-up of the 2 km model, until December 2013. Temperature and nitrate concentrations (1.5 μM) of the Romaine River were used as an input to the model. For each subdomain (2 km and 400 m), an initial conditions and open boundary conditions were interpolated from the larger domain (respectively 5 km and 2 km) for salinity, temperature, nitrate, ammonium, diatoms, flagellates, mezozooplankton, microzooplankton, particulate and dissolved organic nitrogen.

2.5.2. The plankton ecosystem model

In the present study, the plankton model of Le Fouest et al. (2005) was used. Model compartments include nitrates (NO_3) and ammonium (NH_4) as nutrients, and two size classes of phytoplankton, large (LP, > 5 μm) and small (SP, < 5 μm). Secondary producers are classified as mesozooplankton (LZ, 200–2000 μm)

Table 2
References for the estimation of zooplankton carbon content.

Size fraction (μm)	References
150–1000	
Calanus spp.	Thor et al. (2005); Cohen and Lough (1981)
Oithona sp.	Thor et al. (2005); Cohen and Lough (1981)
Pseudocalanus sp.	Thor et al. (2005); Cohen and Lough (1981)
Acartia spp.	Thor et al. (2005); Cohen and Lough (1981)
Temora sp.	Nielsen and Andersen (2002); Breteler et al. (1982)
Copepoda nauplii	Thor et al. (2005); G. Winkler (unpublished data)
Harpacticoidea	Uye et al. (2002) for *Microsetella norvegica*
Cladocera	Walve and Larsson (1999)
Cirripedia nauplii	Turner et al. (2001)
Echinodermata larvae	Basch and Pearse (1996)
Polychaeta larvae	Hansen (1999)
Appendicularia	Sato et al. (2001)
>1000	
Calanus spp.	Thor et al. (2005); Cohen and Lough (1981)
Calanus nauplii	Thor et al. (2005); Turner et al. (2001)
Pseudocalanus sp.	Thor et al. (2005); Cohen and Lough (1981)
Temora sp.	Nielsen and Andersen (2002); Breteler et al. (1982)
Eurytemora (similar to *Acartia*)	Thor et al. (2005); Cohen and Lough (1981)
Echinodermata larvae	Basch and Pearse (1996)
Polychaeta larvae	Hansen (1999)
Decapoda larvae	Urzúa and Anger (2013)

and microzooplankton (SZ, 20–200 μm). Two detrital compartments close the nitrogen cycling: particulate and dissolved organic nitrogen (PON and DON, respectively). A close coupling between small phytoplankton and microzooplankton dynamics, autochthonous nitrogen release, and dissolved organic nitrogen (DON) ammonification is assumed to represent the dynamics of the microbial food web. A direct trophic link between large phytoplankton and microzooplankton was added to the model given the importance of microzooplankton grazing on these organisms (Calbet and Landry, 2004). State variables and partial differential equations were the same as those in Le Fouest et al. (2005). Indeed, phytoplankton biomass was converted into carbon units using a molar C/N ratio of 106/16 (Redfield et al., 1963) and a C/chl-a mass ratio of 55 (Rivkin et al., 1996; Sinclair, 1978]. Furthermore, in the present model we explicitly consider the effect of river-derived matter on both shortwave radiation and the vertical attenuation of photosynthetically available radiation (PAR) in the water column. In fact, yellow substances, i.e. non-algal particles and coloured dissolved organic matter (CDOM), dominate light attenuation in coastal waters, thinning the heat deposition layer and reducing phytoplankton productivity (e.g., Zhai et al., 2011; Mei et al., 2010).

Simulations were performed with the same set of parameters used by Le Fouest et al., (2005) (Table 3), except for trophic links between microzooplankton and small phytoplankton, grazing and half-saturation constants, which were modified from Peña (2003) to fit the observations.

The plankton model was run in all three domains; and as mentioned before, the results of the 5 km domain were used to determine initial and boundary conditions for the model in the 2 km domain, which was used to force the 0.4 km model.

Model performance compared to the observations was performed by means of a Taylor diagram (Taylor, 2001) where each modelled variable is normalized with respect to the standard deviation of the corresponding observations for the 0.4 km domain, which fits the area where the field observations are best represented.

2.5.3. Parameterization of PAR attenuation

To account for runoff-derived yellow substances on PAR attenuation in the water column, Le Fouest et al. (2006) proposed an empirical relationship between salinity and the diffuse PAR attenuation coefficient of non-chlorophyllous matter (K_p). Here we derived a region-specific empirical relationship between K_p and salinity that is valid for the study area. Briefly, the light measurements in the water column (PAR(z)) during spring–summer 2013 in the Romaine River estuary were used to derive the diffuse light attenuation coefficient of PAR (K_{PAR}, m^{-1}) by fitting a non-linear model to the equation

$$PAR(z) = PAR(0-)\exp(-K_{PAR}z) \quad (1)$$

where PAR(0-) is the irradiance just below the sea surface (i.e., at z = 0-) obtained from the LI-COR probe in air (PAR(0-) = 0.96*PAR(0+)). PAR(z) was further normalized to account for potential variation in incident PAR during the light profile measurements. K_{PAR} in oceanic waters can be split into three components (Smith and Baker, 1978):

$$K_{PAR} = K_w + K_{bio}Chl - a + K_p \quad (2)$$

where K_w is the attenuation by pure water (0.04 m^{-1}; Morel, 1988), K_p represents the contribution to diffuse attenuation by other non-covarying detritic substances (i.e., yellow substances), and k_{bio} is the chlorophyll-*a*-specific attenuation coefficient due to algae and co-varying material (in m^2 mg^{-1} chl-a), which decreases as a function of chlorophyll-a concentration (chl-*a*) due to the pigment packaging effect (Morel, 1988, Bricaud et al., 1995):

$$k_{bio} = 0.0518\ Chl - a^{-0.572} \quad (3)$$

For each station, K_p was obtained as

$$K_p = K_{PAR} - K_w - k_{bio}Chl\text{-}a \quad (4)$$

Where chl-*a* was measured *in situ*. In order to estimate K_p in the

Table 3
Values of parameters used in the NPZD model.

Symbol		Value; unit	Reference
	Light Field		
K_w	pure seawater attenuation coefficient	0.04 m^{-1}	Morel (1988)
K_p	non-chlorophyllous matter; associated attenuation coefficient	Eq. 6; m^{-1}	fitted
	Phytoplankton		
k3LP	LP half-saturation constant for NO_3 uptake	1 mmol N m^{-3}	Parsons et al. (1984)
k4LP	LP half-saturation constant for NH_4 uptake	0.5 mmol N m^{-3}	
k3SP	SP half-saturation constant for NO_3 uptake	1 mmol N m^{-3}	
k4SP	SP half-saturation constant for NH_4 uptake	0.1 mmol N m^{-3}	
ke	LP and SP half-saturation constant for light use	10 mol photons m^{-2} d^{-1}	Kiefer and Mitchell (1983)
dtmin	LP and SP minimum doubling time	0.5 day	Zakardjian et al. (2000)
$m_{LP,SP}$	LP and SP senescence	0.02 d^{-1}	fitted
sed_{LP}	LP sinking speed	1 m d^{-1}	Smayda (1970)
	Zooplankton		
gmaxMEZ	MEZ maximum grazing rate	0.8 d^{-1}	Peña (2003)
gmaxMIZ	MIZ maximum grazing rate	1.3 d^{-1}	Peña (2003)
iv_{MEZ}	Ivlev parameter of MEZ grazing formulation	0.6 (mmol N m^{-3})$^{-1}$	Peña (2003)
k_{MIZ}	half-saturation constant for MIZ grazing	0.75 mmol N m^{-3}	Peña (2003)
ass_{MEZ}	MEZ assimilation efficiency	70%	Kiørboe et al. (1988)
ass_{MIZ}	MIZ growth efficiency	30%	Riegman et al. (1993)
m_{MEZ}	MEZ mortality	0.05 (mmol N m^{-3} d^{-1})$^{-1}$	fitted
m_{MIZ}	MIZ senescence	0.02 d^{-1}	fitted
eg	DON egestion by MIZ	30%	Lehrter et al. (1999)
ex	NH4 excretion by MEZ	0.05 d^{-1}	Saiz and Alcaraz (1992)
	Detritus		
sed_{PON}	PON sinking speed	100 m d^{-1}	Turner (2002)
fg	PON fragmentation rate	0.05 d^{-1}	Fasham et al. (1990)
rem	DON remineralization rate	0.4 d^{-1}	Packard et al. (2001)

3D model, the data set was split in two salinity classes. The salinity of 26 was chosen for two reasons: 1) it marks a clear break in the relationship between K_p and salinity and 2) Le Fouest et al. (2006)'s model was obtained for salinity between 26 and 32. Fig. 2 shows the relationship between K_p and salinity based on *in situ* observations. Resulting equations were

$$K_p = -0.0296S + 1.45 \text{ for } S < 26 \quad (5a)$$

and

$$K_p = -0.115S + 3.66 \text{ for } S > 26 \quad (5b)$$

In sum, the 3D simulations use modeled salinity to estimate Kp values (eq. (5)) and modeled chl-a to estimate the phytoplankton-related attenuation using Morel's (1988) equations (eqs (2) and (3)).

2.5.4. Simulating natural and dammed conditions

To evaluate the potential impacts of damming the Romaine River compared with the natural river regime, an additional simulation was done. For this comparison, the simulation was forced in accordance with the management of the Romaine runoff. The management has several restrictions of salmon rivers to follow, i.e. the winter discharges need to be constrained between 140 and 500 $m^3 s^{-1}$ and maintaining a spring freshet (Saucier et al., 2007).

2.6. Statistical analyses

The results of the discrete sampling were analyzed using two-way analysis of variance (ANOVA) comparing depths and dates for the different stations. For the different plankton groups, the same analysis was used to contrast modelled and observed results for the different months and sampling stations. In all cases, ANOVAs were followed by post-hoc Tukey's HSD (Honest Significant Difference) tests to compare means.

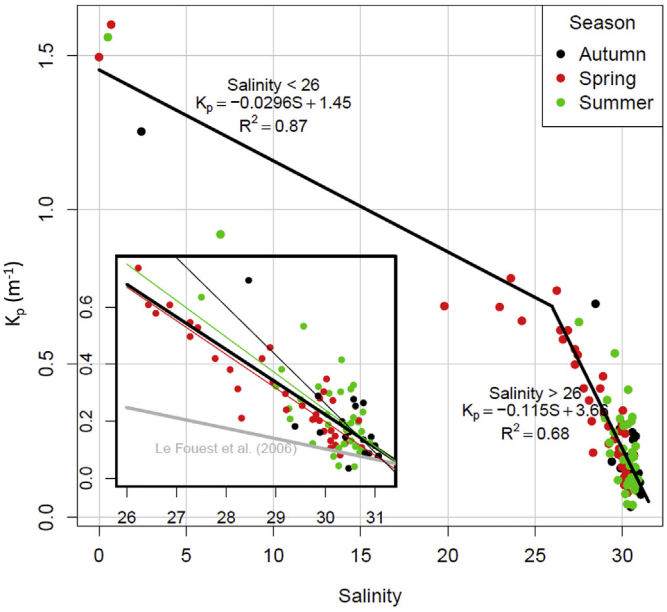

Fig. 2. Scatterplot of K_p versus salinity for the study area. The inset shows the relationships for the three seasons sampled (spring = red-thin, summer = green-thin, autumn = black-thin, all seasons = black-thick) as compared to Le Fouest et al. (2006) relationship for the EGSL (grey-thick). (For interpretation of the references to colour in this figure legend, the reader is referred to the Web version of this article.)

3. Results

3.1. Discrete observations and comparison with model output

3.1.1. Salinity and temperature

The capacity of the model to reproduce monthly averaged data was similar for April and May, on one hand, and from June to September, on the other hand (not shown). Hence, Taylor diagrams (Fig. 3) are presented for each of these two periods: from April to May and from June to September. Surface salinities showed the influence of freshwater runoff at all stations, especially after the spring freshet (early June), with surface values ranging from 0 to 18 for stations P1 to P6 and from 25 to 29 for stations P7 to P10. Therefore, in order to compare the observations with model performance, we separated surface salinity and temperature (above 15 m) from deep waters (below 15 m). In addition, to account for the large variability in surface salinities and to avoid spurious correlations resulting from extreme values such as observed close to the Romaine River mouth, we further considered the comparison between observations and model results for salinities below 10 separated from the rest. The Taylor diagram (Fig. 3) shows that normalized standard deviation for salinity and temperature are relatively close to 1 (between 0.69 and 1.07), except for surface salinity from the June–September period for values less than 10 (1.73).

The lowest temperatures corresponded to the deep waters (45 m) of the April survey. A seasonal warming was observed, maximum temperatures reaching 17 °C and 18 °C in July and August at station P3 at the mouth of the Romaine River. At other stations, highest temperatures occurred in August with values around 10.5 °C (not shown). Mean biases (mean modelled values − mean observed values) are presented on Fig. 3. Model tends to overestimate salinity from April to May (+1.17 for surface water and +1.20 for 15–50 m) and slightly underestimate from June to September (−0.47 for surface waters and −0.26 for 15–50 m). For low salinities, which were found only in surface waters, biases were similar to the values larger than 10. For water temperature, the mean bias was positive for surface water (+0.26 °C) and negative for 15–50 m (−0.31 °C).

3.1.2. Chlorophyll-a

The averaged chl-*a* concentration in surface waters (1.5 m) was 0.87 ± 0.37 mg chl-*a* m^{-3}, while it was 0.79 ± 0.39 mg chl-*a* m^{-3} at 10% of surface irradiance (no differences were found among depths; $p = 0.66$). While the ANOVA showed significant differences among months ($p < 0.01$), post-hoc comparisons only revealed significant differences for May ($p < 0.01$), when the highest concentrations were measured compared to the rest of the months (2.03 ± 1.22 mg chl-*a* m^{-3}; average of other months: 0.53 ± 0.17 mg chl-*a* m^{-3}). No significant differences in chl-*a* concentrations were evident between stations. Moreover, when P3 was excluded from the analysis, the inner (P4, P7, P2, P5, and P6) and outer (P10 and P8) stations were not different either (not shown). We found a significant correlation between chl-*a* concentrations from the surveys and modelled values ($R^2 = 0.55$; $p < 0.001$). As shown in the Taylor diagram (Fig. 3), the simulated chl-*a* tends to be higher than the observations, with a positive mean bias of 0.41 mg chl-*a* m^{-3}. Modelled chl-*a* is less correlated ($R^2 = 0.55$) to observations than salinity and temperature and the normalized standard deviation is 1.34.

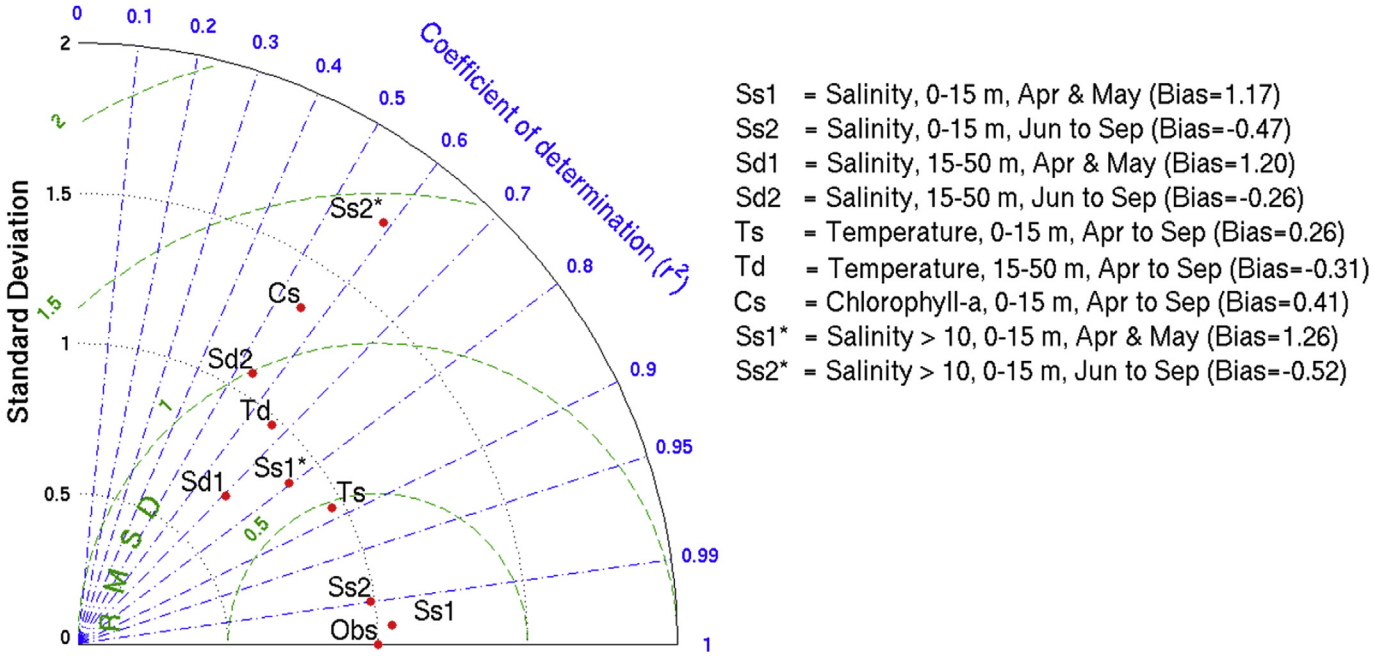

Fig. 3. Taylor diagram showing: coefficient of determination (r^2), root means square deviation and standard deviation, where each modelled variable (salinity, temperature and chlorophyll-a) is normalized with respect to the standard deviation of the corresponding observations for the 0.4 km domain, which fits the area where the field observations are best represented. Data were separated for surface (0–15 m) and deeper (15–50) waters and for spring (April–May) and summer (June–September) as indicated in the legend.

3.2. Continuous observations and comparison with model outputs: time series at buoys locations

3.2.1. Buoys

The continuous buoy observations showed that surface temperature increased from April to September (Fig. 4), starting from ~0 °C in spring and reaching daily average temperatures of around 10 °C in summer, with repeated fluctuations up to 5 °C starting in July. These fluctuations were due to upwelling events induced by winds (which are part of the external model forcings)

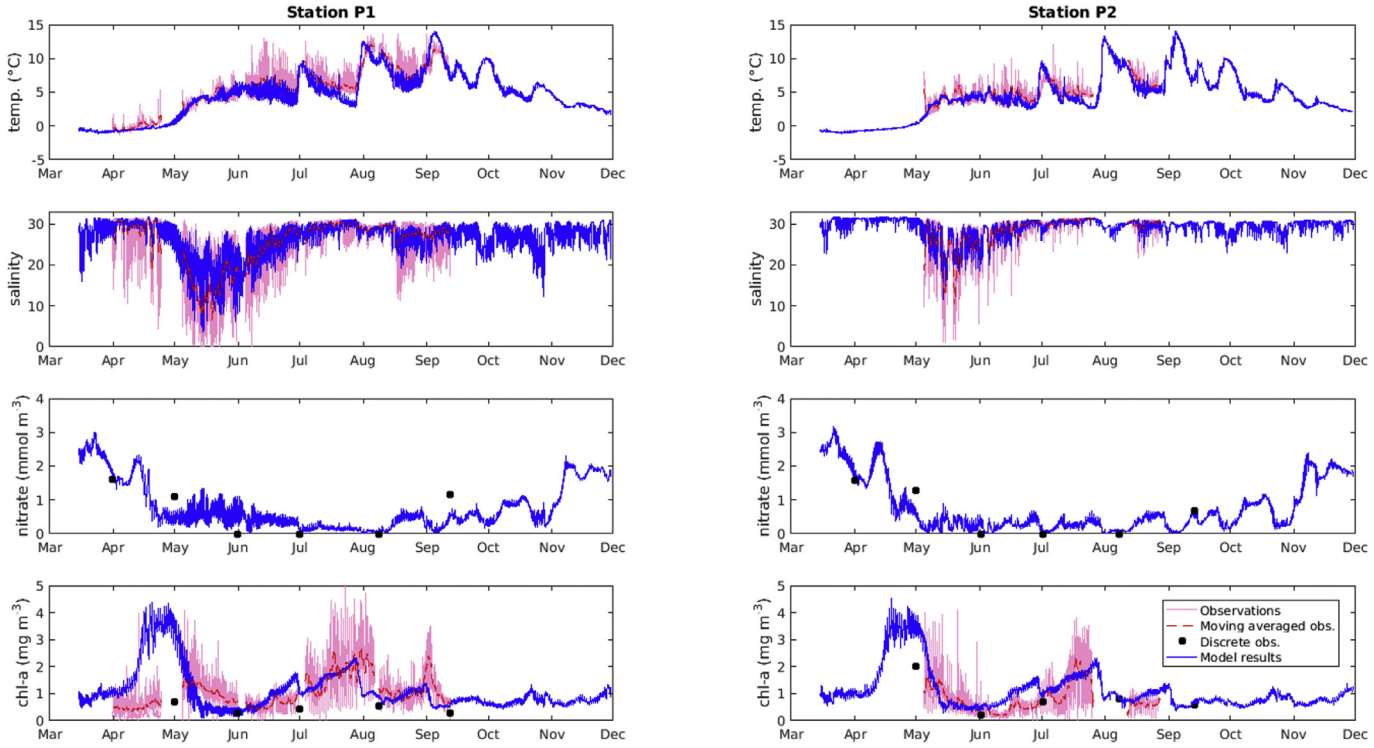

Fig. 4. Observed (pink; daily moving average in red) and modelled (blue) time series: temperature, salinity, nitrate, and chl-a. The results from discrete nitrate and chl-a sampling are also shown (black dots). (For interpretation of the references to colour in this figure legend, the reader is referred to the Web version of this article.)

and were well captured by the model. Modelled data therefore closely agreed with the observed temperature values and temporal variations.

Salinity at both stations showed the effect of the freshwater input during May (spring flood), when minimum values as low as 1 were detected, but otherwise remained around 30 for the rest of the study period (Fig. 4). Fluctuations were more frequent and more intense at P1 than at P2. Again, temporal patterns in modelled salinity values closely followed average daily values measured by the sensors at both stations, reproducing even the highest variability observed at P1.

Discrete nitrate concentrations were well captured by the model, although the relatively high concentrations measured in May were observed in the model about a week before in P1 and some days before in P2. Furthermore, nitrate concentration at station P1 was similarly underestimated at mid-September by the model (Fig. 4).

In vivo fluorescence data, a proxy for chl-*a* concentration, showed a first peak around May, which was also measured in the discrete samples of P2 (Fig. 4). A second peak was observed at the end of July at both P1 and P2; unfortunately, no discrete sampling was done then to compare *in vivo* with lab analyses of chl-*a* concentrations. However, both continuous and discrete data fit the model output, although the number of discrete samples was too small to perform further statistical analyses.

3.2.2. Remote sensing

Although some high K_{PAR} and chl-*a* observed values are not well represented by the model, the general timing and the temporal dynamics were well captured by the model (Fig. 5). On the other hand, from the end of July, the model tends to overestimate K_{PAR} offshore (at RS2 and RS3), which is probably related to a slight underestimation of the salinity. As a result, the model simulated stronger vertical stratification and higher light attenuation, both leading to a slight underestimation of chl-*a* concentration in 27% of the compared points. Note that RS3 was located in the centre of an upwelling area that frequently brought nutrients to the euphotic zone, resulting in high chl-*a* (>2 mg m^{-3} based on satellite data; not shown).

3.3. Plankton community composition

3.3.1. FlowCam analyses

Total cell abundances at the river mouth (station P3) were significantly ($p < 0.01$) different from those at other stations (higher in July and August and lower for all other months). However, no differences among depths ($p = 0.46$) or stations ($p = 0.26$) were evident.

The four plankton classes were averaged for the whole area at the depth of maximum chl-a for comparison with field observations. Biomass of the smallest cell class (SP) was significantly higher than the other size classes ($p < 0.01$) (Fig. 6). Maximum values for both LP and SP were quantified in July, although large variations were observed among stations (note the large error bars in Fig. 6).

3.3.2. Microscopic analysis

Microscopic analysis of total phytoplankton cells showed a distinct pattern for station P3 compared to the rest of the stations, consistent with FlowCam data. While the highest cell numbers were observed in July at P3 (around 3×10^5 cells L^{-1}), maximum

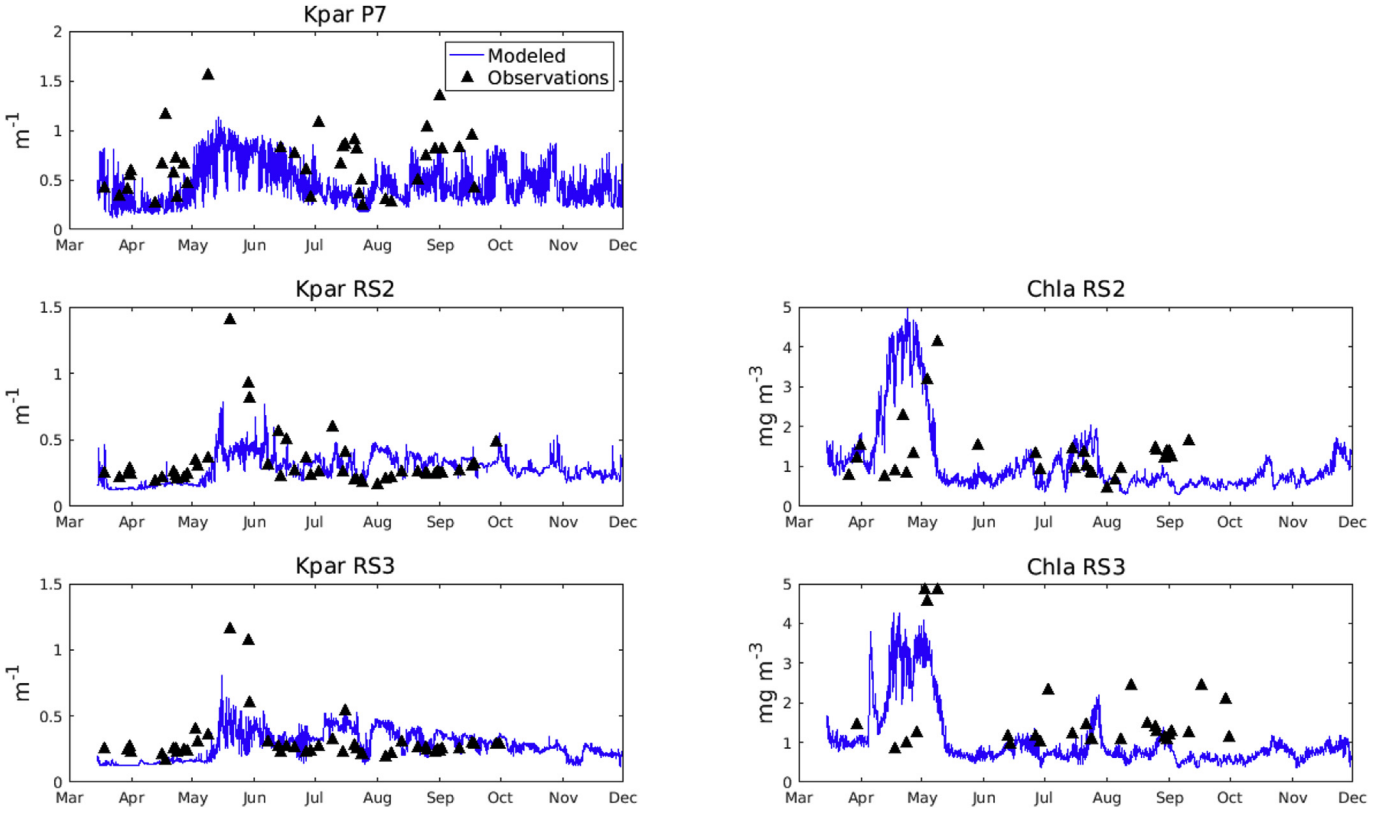

Fig. 5. Comparison between the parameterization (blue) of light attenuation as used in the model and estimated values from satellite data (triangles) for K_{PAR} and chl-a at different locations (see Fig. 1). Satellite-derived chl-a at P7 was not reliable because of stray light (too close to land) and the influence of river runoff, both of which invalidate the ocean color algorithms. (For interpretation of the references to colour in this figure legend, the reader is referred to the Web version of this article.)

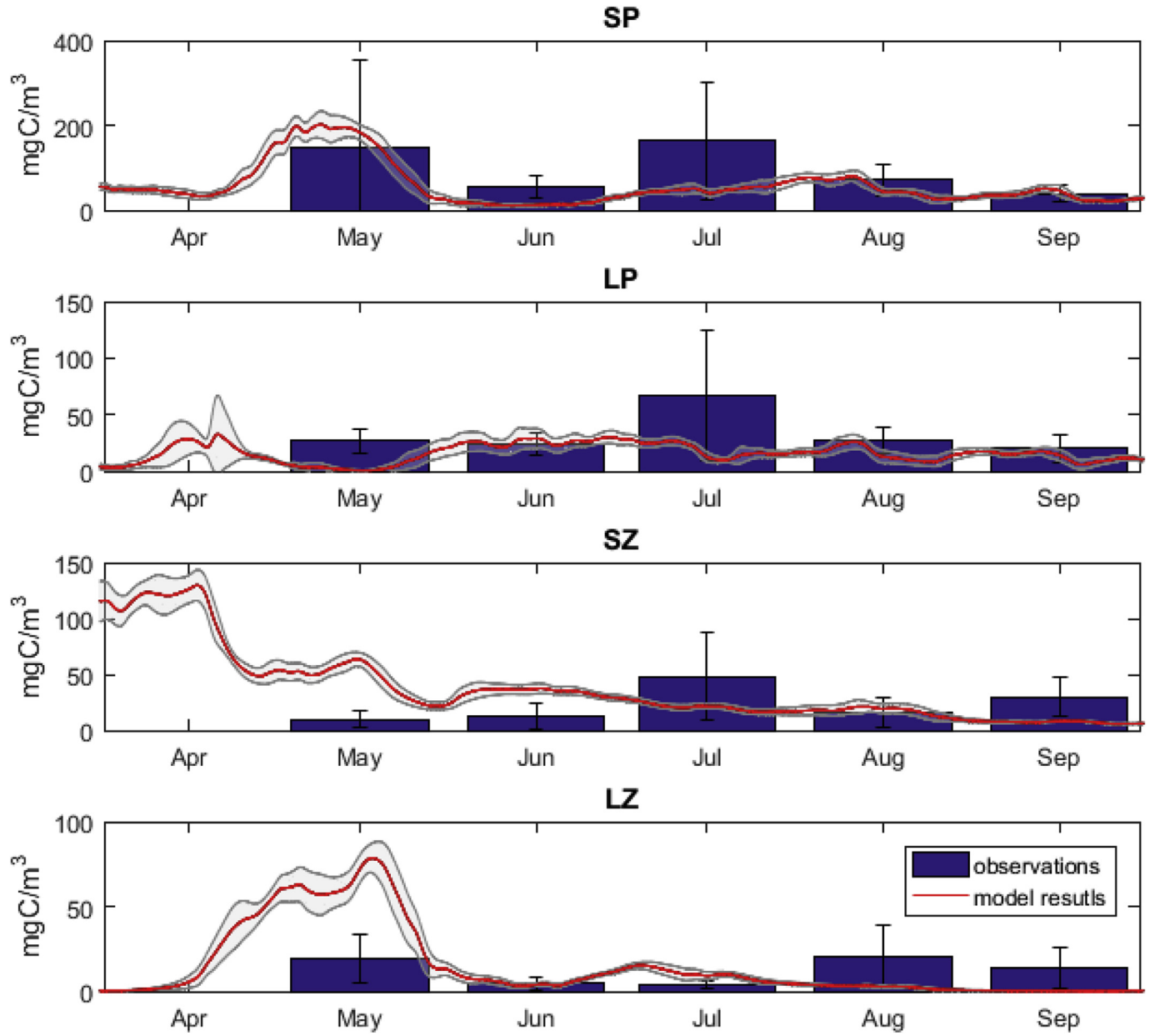

Fig. 6. Biomasses of the different plankton classes as from discrete samples' analysis (bleu bars with error) and from the model output (red line and shaded grey standard deviation). SP: small phytoplankton, LP: large phytoplankton, SZ: small zooplankton, LZ: large zooplankton. (For interpretation of the references to colour in this figure legend, the reader is referred to the Web version of this article.)

values at the remaining stations were observed during August (more than 5×10^5 cells L^{-1}). Phytoplankton composition also differed among stations: P3 was characterized by a dominance of dinoflagellates, which constituted 61% of cells in June and still represented 42% of total cells in September. For the rest of the stations, phytoplankton composition changed from a clearly diatom-dominated assemblage (around 60% of total cell numbers) during April and May to a nanoflagellate-dominated one in August and September. During June and July, 43% dinoflagellates and 39% microflagellates characterized the phytoplankton assemblage.

3.3.3. Zooplankton analyses

A complete list of observed zooplankton taxa is presented in Annex 1. For the 150–1000 μm fraction, maximum zooplankton abundances at all stations were found during the August sampling. These samples were dominated by the calanoid copepods *Eurytemora* spp. and *Pseudocalanus* sp. as well as cyclopoid copepods and Appendicularia. In terms of zooplankton carbon, the highest biomass values were found in April, when up to 95% was due to Cirripedia nauplii. High zooplankton biomasses were also found in August, this time dominated by *Pseudocalanus* sp. and Appendicularia. Maximum abundances of large organisms (>1000 μm) were found during May with a second peak in August. At both sampling dates, the zooplankton community was dominated by cyclopoid and calanoid copepods, both adults and nauplii. In terms of carbon, 87.5% of zooplankton carbon was due to *Calanus* spp. in May and 69% in August. Microzooplankton was higher during summer months (especially during July and September), while mesozooplankton biomass was highest in August.

Although there is a difference between the total carbon

estimated using the FlowCam, microscopic analyses, and the model outputs for the different size classes of plankton, it is important to note that the order of magnitude is similar and often within the limits of uncertainty.

We further compared results of the plankton discrete samples with the model average (±standard deviation) plankton concentration at the depth of chlorophyll maximum for both phytoplankton groups (LP and SP), and averaged over the whole water column for both zooplankton groups (MCZ and MZ), over the 400 m domain, in a continuous manner. The model results for April show that the large phytoplankton bloom took place during that month, for which no discrete samples were available for comparison with the model's output.

The variability observed in LP and SP discrete samples is well represented in the model in May, June, August and September. In July, field samples showed higher phytoplankton abundances and chl-a than the model output. Zooplankton seems underestimated in the field samples, and this will be discussed below.

After comparing observed and modelled plankton biomass, the contrast between the actual forcing and the simulation of the dammed conditions follows.

3.4. Comparing the model results under dammed vs natural conditions

To visualize the differences in the results between natural and dammed regimes over time, the inner part of Mingan archipelago (red square, Fig. 1c) was averaged over the upper 30 m (Fig. 7). Extreme historical (i.e. from 1957 to 2014) runoff values varied from less than 500 up to over 2000 $m^{-3}\,s^{-1}$ (in yellow in Fig. 7a). Under a dammed regime, runoff would be at the lowest values of this range or slightly below it, as in June. Differences between natural and dammed simulations remain small during the period of interest (April to September). In both scenarios, the increase in freshwater runoff observed from May to June, showing a maximum around mid-May, had almost no impact on temperature, but reduced surface salinity from 32 to 29 in dammed conditions compared to 28 under natural conditions. The correlation between water salinity and temperature is partly linked to mixing with saltier and colder underlying water, and partly to the advection of water masses across the boundaries. In both scenarios, the deep mixed layer facilitated the entrainment of nutrients (nitrates) into the surface layer and allowed phytoplankton growth, producing the peak in primary production that was observed in May, without any important difference between both regimes. Zooplankton closely followed this maximum, and a decrease in phytoplankton abundance followed. This decrease is due to a joint effect of the lower nitrate concentrations depleted by phytoplankton growth and to an increase in zooplankton grazing activity. A second peak in chl-*a* was observed by the end of July, after which phytoplankton concentrations remain stable and primary production was below 287 mg C $m^{-2}\,d^{-1}$.

In terms of primary production, which was determined as the sum of new and regenerated phytoplankton production, no major difference in magnitude, timing, or dynamics are notable at this scale (Fig. 7). However, the primary production with regulated runoff, averaged over the inner part of the Mingan Archipelago (red square, Fig. 1c), varied from +41% in March to −15% in July compared to the natural conditions, which correspond to 96 and −55 mg C $m^{-2}\,d^{-1}$, respectively. The average difference in primary production over the spring–summer season between the regulated and natural regime corresponded to an increase of 7.1%.

To depict the spatial distribution of the effects of damming, average monthly anomalies for salinity and primary production were estimated over the 0.4 km grid (Fig. 8). The main differences between simulations under natural and regulated runoff conditions were observed in the salinity anomaly distribution during May (Fig. 8a). The anomaly is shown in kg of salt per square meter integrated over the first 30 m. This unusual display of salt anomaly is intended to show the correlation with the primary production anomaly (Fig. 8b and d). This pattern is closely linked to bathymetry given that values are integrated over the first 30 m for both variables. Changes in the salinity field affect light penetration (eq. (5)). Consequently, in May, the most significant increases in primary production occurred along the northern coast of the islands west of the river mouth (Fig. 8b). Anomaly values integrated over 30 m are between 36 and 72 mg C $m^{-2}\,d^{-1}$ (Fig. 8b). In contrast, in July, primary production decreased west of the river mouth (Fig. 8d), with a maximum decrease of 37 mg C $m^{-2}\,d^{-1}$ in primary production. Regarding possible differences in the interpretation of Fig. 7 and 8, Fig. 7 shows absolute values of primary production while Fig. 8 present its anomalies.

Phytoplankton composition also showed some variations between dammed and undammed conditions. Although the area affected was mostly restricted to the coast, an increase in the relative abundance of large phytoplankton compared to small phytoplankton is evident, mainly in May (not shown). The change represents an increase of more than 100% for LP. Both LP and SP decrease in July, by about 75% on average (not shown); it should be noticed that the model failed to accurately reproduce the dynamics of the different phytoplankton compartments (i.e., LP and SP) when compared to the field observations. In any case, the area where these effects were noticeable was restricted to areas near the Romaine River mouth.

4. Discussion

4.1. Comparison between field data and model results

A number of biological models have been coupled to physical models of the EGSL to simulate plankton production (Le Fouest et al., 2005, 2006), krill migration (Sourisseau et al., 2006), copepod dynamics (Maps et al., 2011), and toxic algae (Fauchot et al., 2008). Their capacity to reproduce realistic outcomes was successfully validated with field measurements of temperature, salinity, water level, sea ice, chl-*a*, and nitrates over several time scales (Saucier et al., 2003; Le Fouest et al., 2006).

4.1.1. Discrete and continuous observations

In the present work, modelled temperature and salinity values reproduced almost all observed levels of variability, such as continuous and discrete sampling (Figs. 3 and 4). Although there was a difference in the observed and modelled salinities at peak freshwater flow from the Romaine River (April and early May), the effect was restricted to the station closest to the coast. This is a notable improvement compared to the model of Le Fouest et al. (2005), which—although capable of reproducing the large-scale phytoplankton dynamics for the whole Gulf—was not conceived to reproduce plankton dynamics in small, coastal domains. Furthermore, the new light parameterization through K_{PAR} substantially improved the match between model outputs and observations (not shown). To adequately simulate the light conditions in coastal waters of the Mingan area, a new parameterization of the K_p versus salinity was a necessary step. For example, the intercept of the K_p–salinity relationship in Le Fouest et al. (2005) was 1.19 m^{-1} compared to 1.45 m^{-1} for the study area. At salinities <29, non-chlorophyllous matter (K_p) was responsible for more than 80% of the total PAR attenuation while it sharply fell to ~60% at higher salinities. Those modelled K_{PAR} values were calculated by the numerical model by assuming that attenuation is due to the simulated

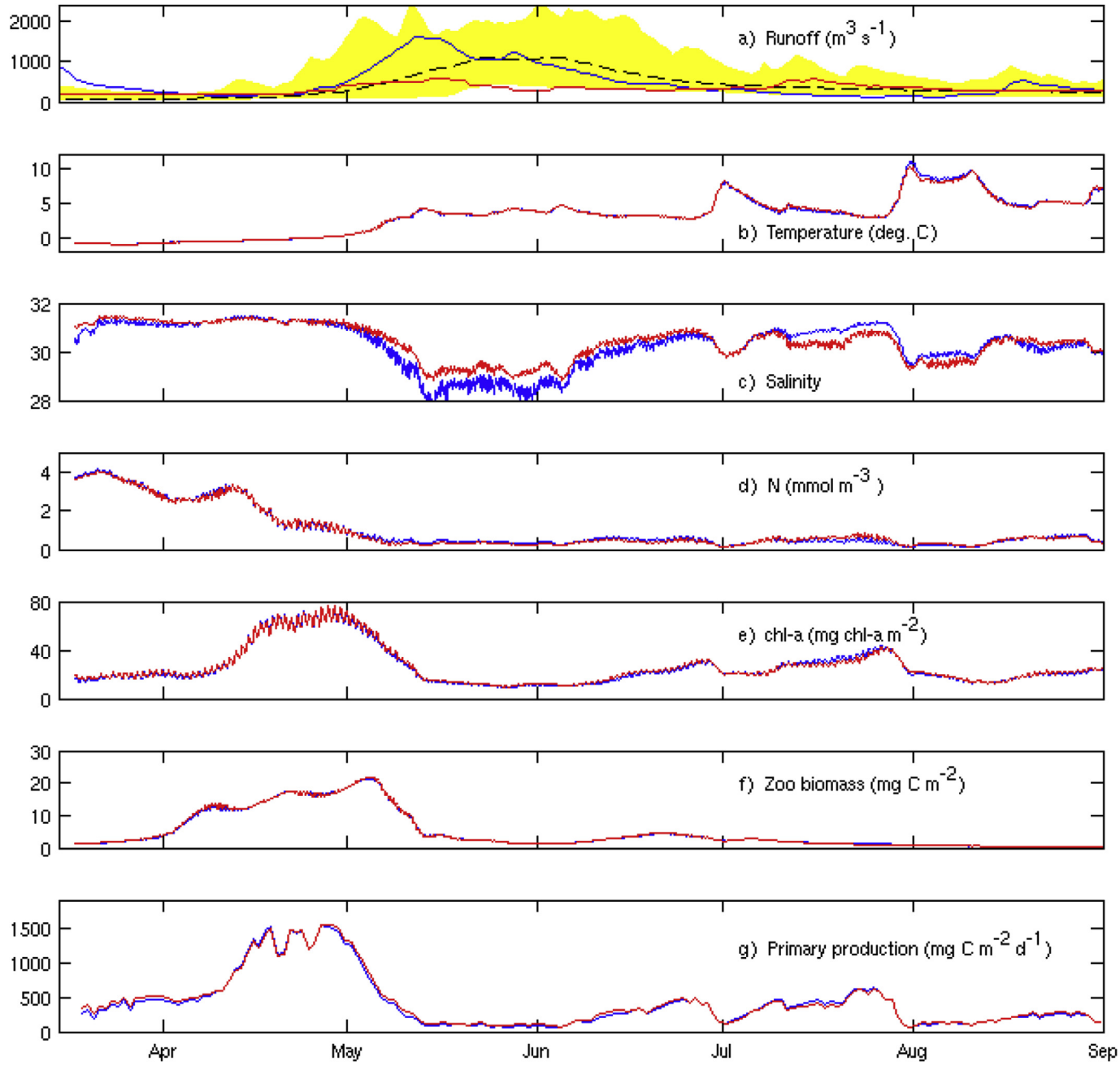

Fig. 7. Temporal evolution of Romaine River daily runoff: a) natural conditions for 2013 (blue), 1957–2014 mean (dashed black), modified (red), and 1957–2014 extremes (yellow) and results of the simulations over the inner part of the Mingan Archipelago domain (red square in Fig. 1c) (natural conditions: blue lines; modified regime: red lines): b) average temperature (0–30 m), c) salinity, d) nitrate concentrations, e) chl-a, f) zooplankton biomass, and g) primary production. (For interpretation of the references to colour in this figure legend, the reader is referred to the Web version of this article.)

chl-*a* concentrations and related to salinity (eqs. (2) and (3)). These coefficients were used to estimate the light available for primary production, but the resulting values could only be compared to satellite values at three points due to a lack of available MODIS-Aqua images for inshore stations. This limitation is often encountered when coastal area are studied (O'Reilly et al., 1998). However, after the end of July, simulated offshore K_{PAR} were overestimated compared to satellite-derived K_{PAR}. This could be due to an excess of freshwater in the domain or simply to a different freshwater end-member that contains less coloured material. This could lead to an underestimation of offshore phytoplankton production. However, this light parameterization provides the best comparison with coastal observations so far.

4.1.2. Plankton community composition

The phytoplankton phenology is generally well reproduced. The temporal variability of the tracer variables is well captured in the model. The timing and magnitude of the phytoplankton bloom were well represented and coherent with previous fields studies (Starr et al., 2002). Even the composition of the phytoplankton assemblage was adequately reproduced in the simulations. For comparison, both Microscopic and FlowCam determinations of cell

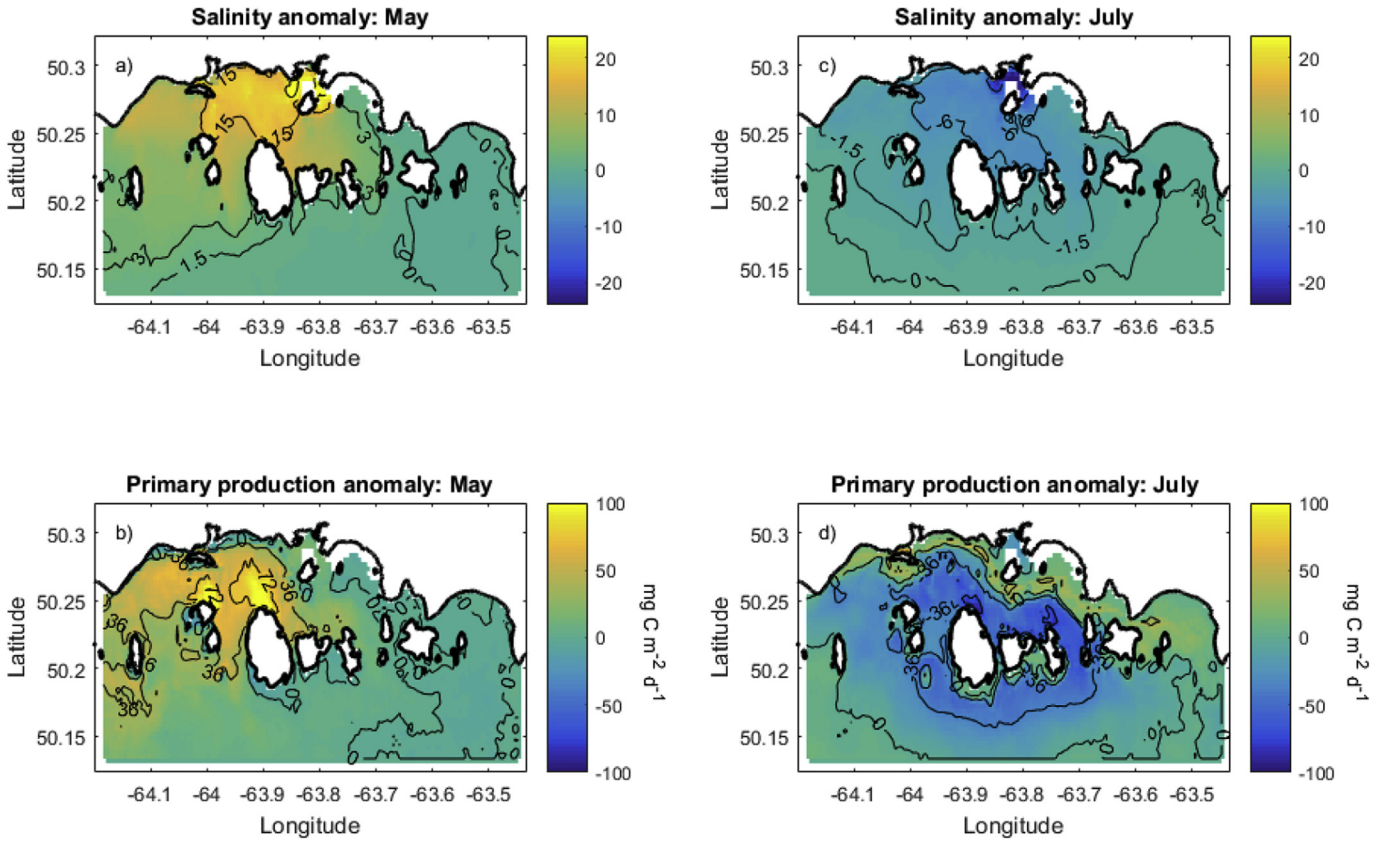

Fig. 8. Salinity anomaly and primary production anomaly averaged over May (a and b), and July (c and d) for the first 10 layers of the model for the inner part of the Mingan Archipelago domain (red square in Fig. 1c). The anomaly is obtained by subtracting the natural from the regulated simulation results. (For interpretation of the references to colour in this figure legend, the reader is referred to the Web version of this article.)

abundances as well as model results were converted into phytoplankton carbon. Although this procedure was performed following the latest recommendations based on the best knowledge available, large imprecisions remain, especially when cells are classified according to size ranges and average values are later estimated. This can lead to large errors, as recognized in Graff et al. (2012). In addition, using constant N:C and C:chl-*a* ratios for transforming the concentrations from the simulation model to compare with the data adds additional sources of error that are not insignificant (Geider et al., 1997). These ratios are known to vary with season, time of day, and species composition of the phytoplankton assemblages (Sathyendranath et al., 2009). A recent modelling study for the Canadian Arctic showed that good results were attained by varying C:chl-*a* ratios between 17 and 73 g g^{-1} for LP and between 10 and 40 g g^{-1} for SP (Le Fouest et al., 2013).

Comparisons of the different components of plankton abundances between field measurements and model results show some differences. This is not surprising, since samples used for microscopic and FlowCam analyses reflect plankton composition on a certain date and time, and it is well known that small-scale hydrographic fluctuations and patchiness among other processes can greatly affect sample composition. In addition, microscopy and FlowCam techniques are not equally effective for identifying all types of organisms. While inverted microscopy is adequate for the determination of microplanktonic species (both microphytoplankton and microzooplankton), it is less accurate for the quantification of nano- and picoplankton. The opposite is true for the FlowCam: due to the small volumes analyzed, it is less accurate for counting larger and rarer organisms. Moreover, although the model can be "sampled" at the exact coordinates and the same dates and times as the discrete sampling events, small-scale hydrographic features that might affect the abundance of the different plankton group are not easily represented.

Plankton composition revealed by microscopic and FlowCam analyses showed the succession of dominant groups similar to what has been described for the Gulf of St. Lawrence (Savenkoff et al., 2000). However, both the chl-*a* data and the plankton composition indicate that sampling was performed at the end of the spring bloom, when large phytoplankton cells are almost completely replaced by small cells. The addition of the trophic link between microzooplankton and large phytoplankton was largely responsible for our ability to adequately reproduce this situation for all months except in the stations most close to the coast. This link has been recently recognized as essential in our understanding of food web dynamics (Calbet and Landry, 2004; Irigoien et al., 2005). Contrasting field samples to model outputs in dynamic areas can be biased by many factors, including small scale patchiness in plankton distribution that bias sampling both field sampling and data extraction from the model, for comparison, which is evident in the large error bars of both, field and model monthly averages in Fig. 6. Indeed, microphytoplankton blooms are transient, short-lived events (Cloern, 1996) while low phytoplankton biomass, mainly dominated by small phytoplankton cells, characterize most of the phytoplankton growing season. Blooms are the result of a temporal imbalance between adequate growth conditions (in terms of light and nutrients) and top-down control by grazers (Calbet and Landry, 2004; Irigoien et al., 2005). There is a discrepancy between the measured Chl-a and the phytoplankton

carbon as estimated from plankton microscopy and Flow-Cam analyses for July. The high phytoplankton biomass from these analyses is also not reflected in the model output. An explanation for this is that, as mentioned above, strong winds upwelled waters in the area in July, which brought resuspended sediments up in the water column, including diatoms (mainly pennate, and probably from benthic origin) contributing to both LP and SP groups. This process (resuspension from bottom diatoms) is not accounted for in the model; no benthic compartment is currently included in the plankton model. This could be an addition to consider in future modelling efforts. Another important difference between model and observations concerns both zooplankton groups, which presented higher values in the model than in the field samples. This is probably related to the fact that sampling in the field was performed during daytime. The dominant zooplankton groups in the samples (Copepods) are very well known for their behavioural daily vertical migration (DVM) (Plourde et al., 2003). Although DVM is not explicitly considered in the model, zooplankton feeding and parameters reflect the average behaviour of organisms, and the result integrates day and night dynamics. Therefore, we speculate that model results are probably more representative of zooplankton dynamics in the field than the field samples.

4.2. Evaluating impacts of damming on plankton dynamics

Hydroelectric dams alter the natural flow of freshwater to coastal areas, changing flow volume and seasonality (Gough et al., 2005). The present modelling exercise clearly illustrates this, with a reduction in the maximum flow in May and an increase in the minimum flow in July. Variations in flow regimes can greatly affect phytoplankton community structure and functioning in estuaries (Sklar and Browder, 1998). In our simulations, the changes in salinity and primary production we noted when comparing the natural and dammed river regimes showed that the increased primary production observed in May under the modified regime is compensated for in July, when the effects of salinity acted to decrease primary production through light attenuation. Farther from the river mouth, the variations in primary production lessened, indicating that the impact of damming is restricted to an area comparable to one third of the domain. Moreover, considering the inner part of the Mingan Archipelago (red square, Fig. 1c), the difference in production is about 7.1% over the whole spring–summer season.

4.2.1. Limitations of the proposed model

The greatest change in the river flow between natural and regulated river conditions in temperate areas occurs in winter, when the energy demand is highest. Our higher resolution simulations did not account for this change because in the studied area frozen rivers and sea-ice formation are common features, which were not included in our higher resolution models. While larger winter inputs of fresh and relatively warm waters under regulated conditions can reduce river ice and presumably coastal sea ice, it is therefore not clear whether these winter changes will have a significant impact on spring and summer plankton dynamics. Further work is therefore needed to include sea ice and shore ice dynamics in the high resolution models in order to simulate the whole annual cycle.

The present simulations could not take into consideration the species' composition of the phytoplankton community. Bérard-Therriault et al. (1999) listed 499 species of (mostly autotrophic) plankton that have been recorded or might be expected in plankton collections, while Shih et al. (1971) recorded 213 species of zooplankton. It is known that relatively small changes in composition can have an impact on the upper levels of the trophic web and affect carbon cycling in the ocean (Finkel et al., 2009). In this sense, the increase in production observed under the dammed conditions corresponds to an increase in the relative abundance of large phytoplankton (not shown), which is normally associated with a plankton community dominated by diatoms. This could benefit meso- and macrozooplankton communities and ultimately commercially important fish species such as capelin and American plaice (Bourdages et al., 2016) and that greatly depend on primary and secondary resources for growth.

An additional limitation of the present exercise is the fact that several biological parameters in addition to light penetration are affected by changes in salinity. As in most modelling studies, parameters in our simulations are set as constants (see Fasham et al., 1990; Le Fouest et al., 2005). This could have an impact on the estimations around the area most influenced by the river waters. It is known that decreased salinity can have a negative impact on marine phytoplankton species because of osmotically induced oxidative stress (Hernando et al., 2015). Finally, although processes of the microbial loop are considered in the calculations as the rates of nutrient regeneration, bacteria are not included as an explicit compartment. Bacterial abundance could vary as a function of a varying freshwater runoff, and it constitutes an extra food source for microzooplankton. This addition could be included in future simulations.

A limitation of the results could be the changes that damming imposes to some properties such as nitrate concentrations of the Romaine River itself and that could affect the initial conditions of the simulation. However, since the range for the nitrate values measured is narrow, we think that the influence of damming on it will not have a significant influence on the present results. This could be considered in further studies.

5. Conclusion

The stepwise nesting of model grids (starting with a model with 5 km cells, then 2 km, and finally 400 m) adequately reproduces the physical characteristics of the studied environment. This was shown by the relatively small differences found when comparing modelled and observed physical variables in the sampled domain, which corresponds to the area represented by the 400 m resolution grid. Moreover, these differences were also minor when considering some plankton model outputs, such as chl-*a* concentration, which is a proxy for phytoplankton biomass. Overall, the model has a good capacity to reproduce observations. Changes made to the model with respect to K_{PAR} were important for obtaining a more accurate light field and simulated plankton dynamics in coastal and relatively shallow areas subject to riverine inputs. The light attenuation correction provided a light (PAR) field that is adequate for simulating phytoplankton growth and plankton dynamics. In addition, the proportion of large and small phytoplankton cells seemed to be adequately parameterized by including the trophic link between microzooplankton and large phytoplankton, which was absent in the original model of LeFouest et al. (2005). The simulation with a modified freshwater inflow representing a dammed Romaine River scenario showed a 7.1% increase of the primary production averaged over the inner part of the Mingan Archipelago (red square, Fig. 1c). However, this variation was not uniform in space and time: it mostly affected the area near the river mouth, where production was higher in May and lower in July. Both these estimates were probably due to the impact of salinity on light penetration, which, in turn, affected phytoplankton growth and production rates. These results allow us to conclude that the present model is a convenient tool for studying the overall impact of river damming on plankton dynamics, and that it could be used in other similar coastal areas that are also affected by riverine inputs.

However, due to the high level of complexity of marine ecosystem, light attenuation parametrisation and model validation with field data remain a necessary step.

Acknowledgments

We would like to thank Catherine Côté, Louise Émond and Michel Bérubé (Hydro-Québec) for supporting this work. Thanks to Charles Deblois, Maud Demarty, Yvonnick Le Clainche and their co-workers for field work and collaboration with data analysis. We also want to thank Sylvain Leblanc (field work), James Caveen (system analyst), Thomas Jaegler (remote sensing treatments) and great thanks to Jean-Baptiste Favier for identifying and quantifying the zooplankton samples. We would also like to thank two anonymous reviewers for their comments, which largely helped to improve the manuscript.

Annex I. List of zooplankton groups used to classify the organisms present in the samples

Cnidaria (ex. Aglantha)	Neomysis sp.
Ctenophora	Calyptopis (Euphausiacea larvae)
Cirripedia nauplii	Insect
Copepoda nauplii	Halacaridea
Harpactocoida	Chaetognatha
Cyclopoida	Polychaeta larvae
Centropagidae	Polychaeta
Scolecithricidae	Decapoda larvae
Monstrillidae	Gastropoda larvae
Acartia spp.	Bivalvia larvae
Eurytemora spp.	Echinodermata larvae
Temora sp.	Tunicata larvae
Pseudocalanus sp.	Appendicularia
Microcalanus sp.	
Metridia sp.	Fish eggs
Paraeuchaeta sp.	Fish larvae
Calanus spp.	
Ostracoda	
Cladocera (Podon and Evadne)	
Bosmina sp	
Isopoda	
Hyperiidea	

References

Basch, L., Pearse, J., 1996. Consequences of larval feeding environment for settlement and metamorphosis of a temperate echinoderm. Oceanol. Acta 19 (3–4), 273–285.

Bérard-Therriault, L., Poulin, M., Bossé, L., 1999. Guide d'identification du phytoplancton marin de l'estuaire et du Golfe du Saint-Laurent incluant également certains protozoaires, 387 pp. Publication Spéciale Canadienne des Sciences Halieutiques et Aquatiques.

Bourdages, H., Brassard, C., Desgagnés, M., Galbraith, P., Gauthier, J., Légaré, B., Nozères, C., Parent, E., Schwab, P., 2016. Preliminary Results from the Groundfish and Shrimp Multidisciplinary Survey in August 2015 in the Estuary and Northern Gulf of St. Lawrence. DFO Can. Sci. Advis. Sec. Res. Doc. 2016/004 v + 87 p.

Bourque, M.C., Kelley, D.E., 1995. Evidence of wind-driven upwelling in Jacques Cartier Strait. Atmos.-Ocean 33 (4), 621–637.

Breteler, W.K., Fransz, H.G., Gonzalez, S.R., 1982. Growth and development of four calanoid copepod species under experimental and natural conditions. Neth. J. Sea Res. 16, 195–207.

Bricaud, A., Babin, M., Morel, A., Claustre, H., 1995. Variability in the chlorophyll-specific absorption coefficients of natural phytoplankton: analysis and parameterization. J. Geophys. Res.: Oceans 100 (C7), 13321–13332.

Calbet, A., Landry, M.R., 2004. Phytoplankton growth, microzooplankton grazing, and carbon cycling in marine systems. Limnol. Oceanogr. 49 (1), 51–57.

Cloern, J.E., 1996. Phytoplankton bloom dynamics in coastal ecosystems: a review with some general lessons from sustained investigation of San Francisco Bay, California. Rev. Geophys. 34 (2), 127–168.

Cloern, J.E., Foster, S.Q., Kleckner, A.E., 2014. Phytoplankton primary production in the world's estuarine-coastal ecosystems. Biogeosciences 11 (9), 2477–2501.

Cohen, R., Lough, R., 1981. Length-weight relationships for several copepods dominant in the Georges Bank-Gulf of Maine area. J. Northwest Atl. Fish. Sci. 2, 47–52.

Domingues, R.B., Galvao, H., 2007. Phytoplankton and environmental variability in a dam regulated temperate estuary. Hydrobiologia 586 (1), 117–134.

Fasham, M.J.R., Ducklow, H.W., McKelvie, S.M., 1990. A nitrogen-based model of plankton dynamics in the oceanic mixed layer. J. Mar. Res. 48 (3), 591–639.

Fauchot, J., Saucier, F.J., Levasseur, M., Roy, S., Zakardjian, B., 2008. Wind-driven river plume dynamics and toxic Alexandrium tamarense blooms in the St. Lawrence estuary (Canada):A modeling study. Harmful Algae 7 (2), 214–227.

Finkel, Z.V., Beardall, J., Flynn, K.J., Quigg, A., Rees, T.A.V., Raven, J.A., 2009. Phytoplankton in a changing world: cell size and elemental stoichiometry. J. Plankton Res. 32 (1), 119–137.

Gazeau, F., Smith, S.V., Gentili, B., Frankignoulle, M., Gattuso, J.-P., 2004. The European coastal zone: characterization and first assessment of ecosystem metabolism. Estuar. Coast Shelf Sci. 60 (4), 673–694. https://doi.org/10.1016/j.ecss.2004.03.007.

Geider, R.J., MacIntyre, H.L., Kana, T.M., 1997. Dynamic model of phytoplankton growth and acclimation: responses of the balanced growth rate and the chlorophyll a : carbon ratio to light, nutrient-limitation and temperature. Mar. Ecol. Prog. Ser. 148, 187–200.

Gough, W.A., Robinson, C., Hosseinian, R., 2005. The influence of James bay river discharge on churchill, manitoba, sea level. Polar Geogr. 29 (3), 213–223.

Graff, J.R., Milligan, A.J., Behrenfeld, M.J., 2012. The measurement of phytoplankton biomass using flow-cytometric sorting and elemental analysis of carbon. Limnol Oceanogr. Meth. 10 (11), 910–920.

Hansen, B.W., 1999. Cohort growth of planktotrophic polychaete larvae - are they food limited? Mar. Ecol. Prog. Ser. 178, 109–119.

Hernando, M., Schloss, I.R., Malanga, G., Almandoz, G.O., Ferreyra, G.A., Aguiar, M.B., Puntarulo, S., 2015. Effects of salinity changes on coastal Antarctic phytoplankton physiology and assemblage composition. J. Exp. Mar. Biol. Ecol. 466, 110–119.

Hillebrand, H., Dürselen, C.D., Kirschtel, D., Pollingher, U., Zohary, T., 1999. Biovolume calculation for pelagic and benthic microalgae. J. Phycol. 35 (2), 403–424.

Hydro-Québec, 2007. Complexe de la Romaine – Étude d'impact sur l'environnement. 10 volumes et annexes, 10-12-2015. http://www.hydroquebec.com/romaine/documents/etude.html. http://www.hydroquebec.com/romaine/pdf/ei_volume09.pdf.

Irigoien, X., Flynn, K.J., Harris, R.P., 2005. Phytoplankton blooms: a 'loophole'in microzooplankton grazing impact? J. Plankton Res. 27 (4), 313–321.

Jaegler, T., 2014. Variabilité spatiale et temporelle des propriétés optiques et chimiques de la matière organique dissoute dans les rivières de la Côte-Nord, Québec, Canada. Master Thesis. Université du Québec à Rimouski, Département de biologie, chimie et géographie, Rimouski, Québec, 181 p.

Kiefer, D.A., Mitchell, B.G., 1983. A simple, steady state description of phytoplankton growth based on absorption cross section and quantum efficiency. Limnol. Oceanogr. 28, 770–776.

Kiørboe, T., Møhlenberg, F., Tiselius, P., 1988. Propagation of planktonic copepods: production and mortality of eggs. Hydrobiologia 167/168, 219–225.

Le Fouest, V., Zakardjian, B., Saucier, F.J., Starr, M., 2005. Seasonal versus synoptic variability in planktonic production in a high-latitude marginal sea: the Gulf of St. Lawrence (Canada). J. Geophys. Res. 110 (9), 1–21.

Le Fouest, V., Zakardjian, B., Saucier, F.J., Cizmeli, S.A., 2006. Application of SeaWiFS- and AVHRR-derived data for mesoscale and regional validation of a 3-D high-resolution physical–biological model of the Gulf of St. Lawrence (Canada). J. Mar. Syst. 60 (1–2), 30–50.

Le Fouest, V., Zakardjian, B., Xie, H., Raimbault, P., Joux, F., Babin, M., 2013. Modeling plankton ecosystem functioning and nitrogen fluxes in the oligotrophic waters of the Beaufort Sea, Arctic Ocean: a focus on light-driven processes. Biogeosciences 10 (7), 4785–4800.

Lee, Z., Carder, K.L., Arnone, R.A., 2002. Deriving inherent optical properties from water color: a multiband quasi-analytical algorithm for optically deep waters. Appl. Optic. 41 (27), 5755–5772.

Lee, Z., Carder, K.L., Arnone, R.A., 2005. A model for the diffuse attenuation coefficient of downwelling irradiance. J. Geophys. Res.: Oceans 110 (C2).

Lehrter, J.C., Pennock, J.R., McManus, G.B., 1999. Microzooplankton grazing and nitrogen excretion across a surface estuarine ecoastal interface. Estuaries 22, 113e125.

Maps, F., Zakardjian, B.A., Plourde, S., Saucier, F.J., 2011. Modelling the interactions between the seasonal and diel migration behaviors of Calanus finmarchicus and the circulation in the Gulf of St. Lawrence (Canada). J. Mar. Syst. 88 (2), 183–202.

Mei, Z.-P., Saucier, F., Le Fouest, V., Zakardjian, B., Senneville, S., Xie, X., Starr, M., 2010. Effects of coloured dissolved organic matter (CDOM) and temperature on primary and secondary productions of Gulf of St. Lawrence : insights from 3-D coupled physics-NPZD model. Continent. Shelf Res. 30, 2027–2042.

Menden-Deuer, S., Lessard, E.J., 2000. Carbon to volume relationships for dinoflagellates, diatoms, and other protist plankton. Limnol. Oceanogr. 45 (3), 569–579.

Montagnes, D.J., Berges, J.A., Harrison, P.J., Taylor, F., 1994. Estimating carbon, nitrogen, protein, and chlorophyll a from volume in marine phytoplankton. Limnol. Oceanogr. 39 (5), 1044–1060.

Morel, A., 1988. Optical modeling of the upper ocean in relation to its biogenous matter content (case I waters). J. Geophys. Res. 93 (C9), 10749–10768. https://doi.org/10.1029/JC093iC09p10749.

Nielsen, T., Andersen, C., 2002. Plankton community structure and production along a freshwater-influenced Norwegian fjord system. Mar. Biol. 141 (4), 707–724.

O'Reilly, J.E., Maritorena, S., Mitchell, B.G., Siegel, D.A., Carder, K.L., Garver, S.A., et al., 1998. Ocean color chlorophyll algorithms for SeaWiFS. J. Geophys. Res.: Oceans 103 (C11), 24937–24953.

Packard, T., Chen, W., Blasco, D., Savenkoff, C., Vézina, A.F., Tian, R.C., St-Amand, L., Roy, S., Lovejoy, C., Klein, B., Therriault, J.-C., Legendre, L., Ingram, R.G., 2001. Dissolved organic carbon in the gulf of St. Lawrence. Deep Sea Res., Part II 47, 435–459.

Parsons, T., Takahashi, M., Hargrave, B., 1984. Biological Oceanographic Processes, third ed. Pergamon Press, England, p. 330.

Pellerin, P., Ritchie, H., Saucier, F.J., Roy, F., Desjardins, S., Valin, M., Lee, V., 2004. Impact of a two-way coupling between an atmospheric and an ocean-ice model over the Gulf of St. Lawrence. Mon. Weather Rev. 132 (6), 1379–1398.

Peña, M.A., 2003. Modelling the response of the planktonic food web to iron fertilization and warming in the NE subarctic Pacific. Prog. Oceanogr. 57 (3), 453–479.

Plourde, J., Therriault, J.C., 2004. Climate variability and vertical advection of nitrates in the Gulf of St. Lawrence, Canada. Mar. Ecol. Prog. Ser. 279, 33–43.

Plourde, S., Joly, P., Runge, J., Dodson, J., Zakardjian, B., 2003. Life cycle of Calanus hyperboreus in the lower St. Lawrence Estuary and its relationship to local environmental conditions. Mar. Ecol. Prog. Ser. 255, 219–233. Retrieved from: http://www.jstor.org/stable/24866961.

Redfield, Alfred C., 1963. The influence of organisms on the composition of seawater. Sea 2, 26–77.

Riegman, R., Kuipers, B.-R., Noordeloos, A.-A.M., Witte, J.I.J., 1993. Size-differential control of phytoplankton and the structure of plankton communities. Neth. J. Sea Res. 31, 255–326.

Rivkin, Richard B., Anderson, M.R., Lajzerowicz, C., 1996. Microbial processes in cold oceans. I. Relationship between temperature and bacterial growth rate. Aquat. Microb. Ecol. 10 (3), 243–254.

Ruddick, K.G., Ovidio, F., Rijkeboer, M., 2000. Atmospheric correction of SeaWiFS imagery for turbid coastal and inland waters. Appl. Optic. 39 (6), 897–912.

Ruddick, K.G., De Cauwer, V., Park, Y.J., Moore, G., 2006. Seaborne measurements of near infrared water-leaving reflectance: the similarity spectrum for turbid waters. Limnol. Oceanogr. 51 (2), 1167–1179.

Saiz, E., Alcaraz, M., 1992. Enhanced excretion rates induced by small-scale turbulence in Acartia (Copepoda: calanoida). J. Plankton Res. 14, 681–689.

Sathyendranath, S., Stuart, V., Nair, A., Oka, K., Nakane, T., Bouman, H., Platt, T., 2009. Carbon-to-chlorophyll ratio and growth rate of phytoplankton in the sea. Marine Ecolol. Prog. Ser. 383 (7).

Sato, R., Tanaka, Y., Ishimaru, T., 2001. House production by Oikopleura dioica (Tunicata, Appendicularia) under laboratory conditions. J. Plankton Res. 23 (4), 415–423.

Saucier, F.J., Roy, F., Gilbert, D., Pellerin, P., Ritchie, H., 2003. Modelling the formation and circulation processes of water masses and sea ice in the Gulf of St. Lawrence, Canada. J. Geophys. Res. Oceans 108 (C8), 3269–3289.

Saucier, F.J., Senneville, S., Prinsenberg, S., Roy, F., Smith, G., Gachon, P., Laprise, R., 2004. Modelling the Sea ice-ocean seasonal cycle in hudson bay, foxe basin and hudson strait, Canada. Clim. Dynam. 23 (3), 303–326.

Saucier, F., Zarkardjian, B., Senneville, S., Le Fouest, V., 2007. Étude de l'effet de l'aménagement du complexe hydroélectrique de la rivière Romaine sur les conditions biologiques et physiques du chenal de Mingan à l'aide d'un simulateur numérique tridimensionnel à haute définition. Institut des Sciences de la Mer, Université du Québec à Rimouski. http://www.bape.gouv.qc.ca/sections/mandats/La%20Romaine/documents/PR8.4/PR8.4.pdf, 10-12-2015.

Savenkoff, C., Vézina, A.F., Roy, S., Klein, B., Lovejoy, C., Therriault, J.C., et al., 2000. Export of biogenic carbon and structure and dynamics of the pelagic food web in the Gulf of St. Lawrence Part 1. Seasonal variations. Deep Sea Res. Part II Top. Stud. Oceanogr. 47 (3), 585–607.

Shih, C.T., Figueira, A.J., Grainger, E.H., 1971. A Synopsis of Canadian Marine Zooplankton. Fisheries Research Board of Canada Ottawa.

Sinclair, Michael, 1978. "Summer phytoplankton variability in the lower St. Lawrence estuary. J. Fish. Res. Board Can. 35 (9), 1171–1185.

Sklar, F.H., Browder, J.A., 1998. Coastal environmental impacts brought about by alterations to freshwater flow in the Gulf of Mexico. Environ. Manag. 22 (4), 547–562.

Smayda, T.J., 1970. The suspension and sinking of phytoplankton in the sea. Oceanogr. Mar. Biol. Rev. 8, 353–414.

Smith, C., Baker, K.S., 1978. Optical classification of natural waters. Limnol. Oceanogr. 23 (2), 260–267.

Sourisseau, M., Simard, Y., Saucier, F.J., 2006. Krill aggregation in the St. Lawrence system, and supply of krill to the whale feeding grounds in the estuary from the gulf. Mar. Ecol. Prog. Ser. 314, 257–270.

Spall, M.A., Holland, W.R., 1991. A nested primitive equation model for oceanic applications. J. Phys. Oceanogr. 21 (2), 205–220.

Starr, M., St-Amand, L., Bérard-Therriault, L., 2002. State of Phytoplankton in the Estuary and Gulf of St. Lawrence during 2001. Canadian Science Advisory Secretariat Research Document 2002/067.

Taylor, K.E., 2001. Summarizing multiple aspects of model performance in a single diagram. J. Geophys. Res.: Atmosphere 106 (D7), 7183–7192.

Thor, P., Nielsen, T.G., Tiselius, P., Juul-Pedersen, T., Michel, C., Møller, E.F., et al., 2005. Post-spring bloom community structure of pelagic copepods in the Disko Bay, Western Greenland. J. Plankton Res. 27 (4), 341–356.

Turner, J.T., 2002. Zooplankton faecal pellets, marine snow and sinking phytoplankton blooms. Aquat. Microb. Ecol. 27, 57–102.

Turner, J.T., Levinsen, H., Nielsen, T.G., Hansen, B.W., 2001. Zooplankton feeding ecology: grazing on phytoplankton and predation on protozoans by copepod and barnacle nauplii in Disko Bay, West Greenland. Mar. Ecol. Prog. Ser. 221, 209–219.

Urzúa, Á., Anger, K., 2013. Seasonal variations in larval biomass and biochemical composition of brown shrimp, Crangon crangon (Decapoda, Caridea), at hatching. Helgol. Mar. Res. 67 (2), 267–277.

Utermöhl, H., 1958. Zur vervollkommnung der quantitativen phytoplankton-methodik. Mitt. Int. Ver. Theor. Angew. Limnol. 9, 1–38.

Uye, S., Aoto, I., Onbé, T., 2002. Seasonal population dynamics and production of Microsetella norvegica, a widely distributed but little-studied marine planktonic harpacticoid copepod. J. Plankton Res. 24 (2), 143–153.

Walve, J., Larsson, U., 1999. Carbon, nitrogen and phosphorus stoichiometry of crustacean zooplankton in the Baltic Sea: implications for nutrient recycling. J. Plankton Res. 21 (12), 2309–2321.

Zakardjian, B., Gratton, Y., Vézina, A.F., 2000. Late spring phyto-plankton bloom in the Lower St. Lawrence Estuary: the flushing hypoth-esis revisited. Mar. Ecol. Prog. Ser. 192, 31–48.

Zhai, L., Tang, C., Platt, T., Sathyendranath, S., 2011. Ocean response to attenuation of visible light by phytoplankton in the Gulf of St. Lawrence. J. Mar. Syst. 88 (2), 285–297.